


Transportation and coherent structures in MHD turbulent channel flow subject to uniform streamwise and spanwise magnetic fields

Olivier Doche ^{*}

Univ. Grenoble Alpes, CNRS, Grenoble INP, SIMAP, F-38000 Grenoble, France

Sedat Tardu 

Univ. Grenoble Alpes, CNRS, Grenoble INP, LEGI, F-38000 Grenoble, France

Jonathan Schillings 

Univ. Grenoble Alpes, CNRS, Grenoble INP, LEPMI, F-38000 Grenoble, France

Amandine Capogna 

Univ. Grenoble Alpes, CNRS, Grenoble INP, SIMAP, F-38402 Grenoble, France



(Received 31 March 2021; accepted 30 August 2021; published 14 September 2021)

This investigation concerns the response of wall turbulences in a channel flow to uniform streamwise and spanwise magnetic fields through direct numerical simulations. More than 20 flow cases with different Stuart numbers were considered. It is found that the spanwise magnetic field leads to flow relaminarization at Stuart numbers significantly smaller than the streamwise magnetic field. The explanation of this phenomenon is not straightforward, and a deep analysis of the fine turbulence structure is needed for a clear understanding. This is achieved in a first step by considering Reynolds shear stress transport equations. It is shown that there are source and destruction terms directly related to the magnetic field. The destruction term overcomes the source terms under the spanwise magnetic field, leading to significant drag reduction once the Stuart number exceeds a critical value. The source term is not negligible and retards the relaminarization under the streamwise magnetic field. Subsequently, the conditional averages of the fluctuating velocity field and the electric current deduced from the near wall coherent quasistreamwise vortices are discussed in detail. The electric current field is decomposed into an electromotive and conductive part. Their conditional averages are analyzed separately, in order to shed light on the topological differences. It is further shown that the quasistreamwise vortex paradigm allows an easy way to analyze the results leading to pertinent interpretations.

DOI: [10.1103/PhysRevFluids.6.094605](https://doi.org/10.1103/PhysRevFluids.6.094605)

I. INTRODUCTION

Flow control by magnetic fields at low magnetic Reynolds numbers has several applications in technological processes wherein electro-conducting fluids are involved. The magnetohydrodynamic (MHD) body force interacts directly with the turbulent flow field, and the resulting manipulation is nonintrusive. Fraim and Heiser [1] showed in the early 1960s that a magnetic field aligned with the mean flow can lead to significant drag reductions up to relaminarization providing that the intensity of the imposed magnetic field is large enough. Extensive work was also devoted to the reaction of

^{*}olivier.doche@simap.grenoble-inp.fr

wall-bounded turbulent flows to uniform transverse magnetic field nonaligned with the mean flow. In the late 1960s and early 1970s, several experiments were conducted in the liquid metal MHD facility of Purdue University's Magneto-Fluid-Mechanic Laboratory. These investigations were focused on the MHD manipulation of turbulent internal flows (mercury) and essentially described the drag coefficient evolution, the mean velocity, and the associated statistics of the fluctuating quantities in a wide range of Reynolds and Hartmann numbers [2–4]. Consideration was also given to the distinct behaviors of the turbulent flow field submitted to magnetic fields. One of them is the persistence of paradoxical residual disturbances in the relaminarized regime. Branover and Gershon [5] have shown that, because of the strong anisotropy induced by the magnetic field, the large-scale disturbances in the entry region of a duct are stretched, enhanced, and sustained in the field direction. This leads to the weakening of the interactions between velocity and magnetic fields. Numerical simulations have also helped to increase understanding. Lee and Choi [6] extensively investigated the effect of magnetic field orientation on the fine structure of turbulence in a fully developed turbulent channel flow. They have shown that a spanwise or wall normal magnetic field is much more efficient than the parallel one in terms of turbulent drag reduction. Based on the previous work of Krasnov *et al.* [7], Boeck *et al.* [8] conducted a parametric study in terms of Reynolds and Hartman numbers to investigate the response of the region subject to a wall normal magnetic field.

A wall normal uniform magnetic field imposed between two virtually infinite parallel walls is known as a Hartmann flow [9]. In this configuration, the magnetic field interacts directly with the mean flow, which asymptotically tends to become flat in the bulk region as the Hartmann number increases. This velocity-magnetic field interaction generates a spanwise electrical current which flows along the parallel walls (also called sidewalls or Shercliff layers) in the case of a duct configuration. Bulk opposite electrical current flows is set up in a region close to the wall by continuity. As a result, the mean velocity gradient increases at the wall. This configuration has been, for example, numerically studied either with direct numerical simulations [6,10] or with large eddy simulations [11]. As the mean velocity interacts with the magnetic field, the Hartmann flow is not a good candidate for a direct investigation of the effect of magnetic forces on turbulent fluctuations. Turbulent fluctuations are closely related to the existence of coherent structures evolving in the inner layer of a turbulent channel flow. These dominant structures are found mostly in the buffer layer and characterized by a significant elongation in the longitudinal direction. These quasistreamwise vortices have a key role in the regeneration mechanism involved in the near wall cycle of turbulence [12–14].

The present investigation deals with the canonical fully developed turbulent channel flow, corresponding to the channels with infinitely small aspect ratios. The sidewall effects inducing the Shercliff layers present in a duct flow are in fact neglected [15]. The base flow is fully turbulent, and the transition to turbulence aspects are obviously out of the scope of this study [16]. Moreover, the imposed magnetic field is strictly parallel to the wall in the present investigation, and there are no Hartmann layers. Consequently, there is no mean Lorentz force, and the mean flow does not directly interact with the magnetic field. The streamwise Reynolds averaged Navier-Stokes equation stays therefore identical to that of the canonical turbulent channel flow.

The aim of this investigation is to contribute to the understanding of the near wall turbulence submitted to a streamwise or spanwise magnetic field. It will be shown, *inter alia*, that the spanwise magnetic field is more efficient in terms of drag reduction than the streamwise one, according to past research. The first alternative idea here is to attempt to understand these phenomena through the analysis of the turbulent shear stress transport equations. Moreover, it is well known that the near wall coherent structures play a fundamental role in the transport process. Thus, the second alternative approach of this study lies in the analysis of the conditional averages of the electric current fields and the MHD flow characteristics. We clearly claim that a clear understanding of the MHD effects occurring in turbulent near wall flows is not possible without considering these elements.

The paper is organized as follows. The governing equations and the details concerning the direct numerical simulations follow in the next section. The flow and electric current statistics are

discussed in Sec. III, wherein the shear stress transport equations are also analyzed to a considerable extent. Section IV concentrates on the capital role played by the buffer layer coherent structures together with the electric current fields and the coherent MHD events they induce.

II. PROBLEM DESCRIPTION

A. Governing equations

We consider a fully developed turbulent channel flow under the action of a magnetic field \mathbf{B} . MHD flows are governed by the Navier-Stokes equations submitted to the Lorentz force and coupled with the Maxwell equations. In addition, this system is associated with the generalized Ohm law. Therefore, for a Newtonian, incompressible and electro-conducting fluid, the full system can be expressed as

$$\frac{\partial \mathbf{u}}{\partial t} + (\mathbf{u} \cdot \nabla) \mathbf{u} = -\frac{1}{\rho} \nabla p + \nu \nabla^2 \mathbf{u} + \frac{1}{\rho} (\mathbf{j} \times \mathbf{B}), \quad (1)$$

$$\frac{\partial \mathbf{B}}{\partial t} = \nabla \times (\mathbf{u} \times \mathbf{B}) + \frac{1}{\mu \sigma} \nabla^2 \mathbf{B}, \quad (2)$$

where \mathbf{u} denotes the velocity field, p is the pressure, and \mathbf{j} is the electric current density. Physical parameters occurring in the MHD problem are ρ the density, ν the kinematic viscosity, μ the magnetic permeability, and σ the electrical conductivity of the fluid. The set of equations (1) and (2) are coupled with the incompressibility condition of the velocity field ($\nabla \cdot \mathbf{u} = 0$), the solenoidal feature of the magnetic field ($\nabla \cdot \mathbf{B} = 0$), and the Ampère law ($\nabla \times \mathbf{B} = \mu \mathbf{j}$).

This system can be simplified when the magnetic Reynolds number $R_m = \mu \sigma U_{cp} h$, representing the ratio between the advection and the diffusion terms of the magnetic field in Eq. (2), is small enough. Under these circumstances, the magnetic field diffuses instantaneously in the flow without being greatly altered by the induced electrical currents. The nondependency in time of the magnetic field \mathbf{B} (i.e., $\frac{\partial \mathbf{B}}{\partial t} = 0$) is guaranteed in liquid metals when the imposed magnetic fields are of moderate intensity, and more precisely when the Hartmann number is smaller than $\text{Ha} \sim 10^3$ [17]. It is recalled that the Hartmann number is defined as $\text{Ha}^2 = (Bh)^2 (\frac{\sigma}{\rho \nu})$ and represents the ratio of the Lorentz to the viscous forces. Here h denotes the half-height of the channel, while U_{cp} stands for the centerline velocity of the equivalent laminar Poiseuille flow. B stands for the characteristic intensity of the imposed magnetic field. In the remainder of the paper, the quantities are scaled by the shear velocity $u_\tau = \sqrt{\tau_0 / \rho}$ of the unmanipulated fully developed turbulent channel flow and the kinematic viscosity ν . The full system in dimensionless form is

$$\frac{\partial \mathbf{u}}{\partial t} + (\mathbf{u} \cdot \nabla) \cdot \mathbf{u} = -\nabla p + \nabla^2 \mathbf{u} + N_\tau (\mathbf{j} \times \mathbf{B}), \quad (3)$$

$$\nabla^2 \phi = \nabla \cdot (\mathbf{u} \times \mathbf{B}), \quad (4)$$

$$\mathbf{j} = -\nabla \phi + \mathbf{u} \times \mathbf{B}, \quad (5)$$

$$\nabla \cdot \mathbf{u} = 0, \quad (6)$$

where j is normalized by $\sigma B u_\tau$, ϕ stands for the electric potential (normalized by $B h u_\tau$). B is the magnitude of a reference magnetic field, and \mathbf{B} represents the nondimensionalized solenoidal permanent magnetic field.

The relevant nondimensional number appearing in Eq. (3), is a modified Stuart number $N_\tau = (\frac{\text{Ha}}{\text{Re}_\tau})^2$ where $\text{Re}_\tau = \frac{u_\tau h}{\nu}$ is the Kármán number of the unmanipulated flow. Note that here N_τ is based on Re_τ and results from the scaling of the momentum equations in inner variables. Thus, N_τ is different from the Stuart number $N = \frac{\text{Ha}^2}{\text{Re}}$, most commonly used in the literature, where the Re number is based on the centerline (or bulk) velocity. The Stuart number, which is also called the interaction parameter, represents the ratio of the Lorentz forces to the inertial terms.

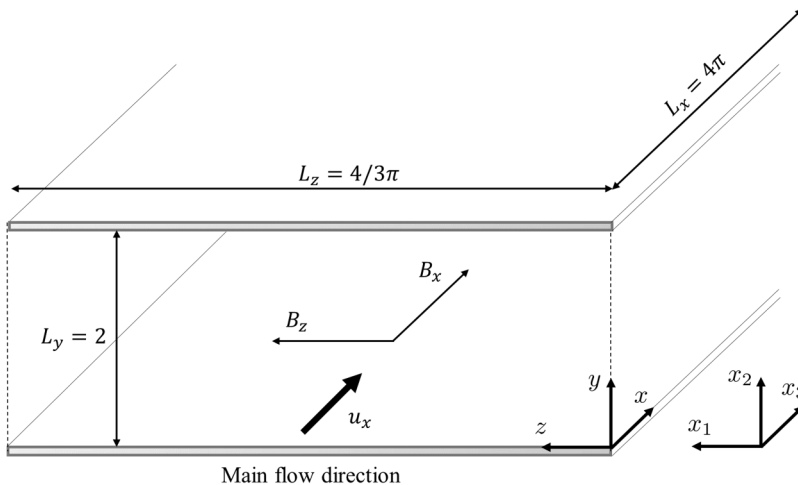


FIG. 1. Computational box and flow configuration. Lengths are scaled by the half channel height h .

The Reynolds number is defined as $\text{Re} = \frac{U_{cp}h}{\nu}$ and is set at 4200 throughout the study. This corresponds to $\text{Re}_\tau = 180$, which is low but is large enough to unveil the fine interactions between the near wall turbulence and the magnetic field. Investigating larger Re numbers is computationally expensive, because the inclusion of the magnetic field increases the computation time roughly by a factor of four compared to the unmanipulated case. We also make clear that more than 20 flow cases have been investigated here.

The results are mainly presented as a function of the Stuart number N_τ , which is the relevant physical parameter. The Ha number is also referred to in the paper from time to time.

The streamwise, wall normal, and spanwise directions are denoted by x , y , and z . The fluctuating velocity components along these directions are u_x , u_y , and u_z , respectively. Occasionally the indicial notation of the shear stress tensor u_{ij} is also used. Time-averaged quantities on homogeneous periodical directions (i.e., the horizontal $[x, z]$ plane) will be denoted by $(\bar{\cdot})$ throughout the paper. We will denote mean flow quantities with uppercase letters and fluctuations with lowercase letters. For the sake of brevity, the root mean squares of the turbulent quantities are denoted by $(\cdot)'$, such as $u'_x = \sqrt{\overline{u_x u_x}}$, $u'_y = \sqrt{\overline{u_y u_y}}$, or $j' = \sqrt{\overline{j j}}$, etc.

B. Direct numerical simulations

We consider a fully developed turbulent channel flow whose dimensions are $[4\pi h, 2h, \frac{4}{3}\pi h]$ respectively in the $[x, y, z]$ directions (see Fig. 1). Periodic boundary conditions on the velocity and electric potential are imposed in the streamwise x and spanwise z directions. We also consider perfectly insulating walls (i.e., $\frac{\partial \phi}{\partial y} = 0$) with no slip ($u_x, u_z = 0$) and no transpiration conditions ($u_y = 0$) on planes located at $y = 0$ and $2h$. In a similar manner to [6], a global condition on mean current is imposed in order to ensure $\iiint_V \mathbf{j} dx dy dz = 0$ on the entire computational box at each time step. The numerical resolution is performed with the DNS code MULTIFAST (e.g., [18, 19]). Spatial numerical operators are expressed by using an *explicit optimized* (EO) finite differences scheme. EO schemes are derived from the dispersion-relation-preserving (DRP) schemes as introduced by Tam and Webb [20]. In contrast to compact scheme discretization, an explicit scheme requires only the function value at the neighboring points in order to approximate the derivatives. Hence, the derivative estimations are direct, while it necessarily implies a matrix inversion in the compact schemes. More technical details about spatial discretization performed with sixth-order EO schemes can be found in Bauer *et al.* [18].

The mesh nodes are distributed uniformly along x and z and refined near the wall in the wall-normal y direction. The mesh size Δy is set to one third of the Kolmogorov scale η near the wall while $\Delta y \approx \eta$ at the centerline. The computational details can be found in the Appendix.

All calculations were performed on a mesh with $257(x) \times 129(y) \times 129(z)$ computational nodes, and the temporal advancement was carried out using a time step $\Delta t = 0.07$.

The turbulent channel flow submitted to the magnetic forcing becomes fully developed after 100 000 time steps starting from the unmanipulated case. Once the flow is established, the computations are extended over 200 000 temporal iterations in order to produce a sufficient amount of data necessary for the statistical convergence. The data are stored at the rate of 20 fields every 10 000 time steps. The results obtained by the DNS-MHD code developed here are in excellent agreement with Krasnov *et al.* [21], who used a pseudospectral DNS at $Re = 13\,300$ and a magnetic field imposed along the spanwise direction with $Ha = 20$ (not shown).

III. MEAN FLOW AND FLUCTUATING VELOCITY FIELD

We will now revisit the effect of Lorentz forces resulting from uniform magnetic fields in the streamwise and spanwise directions. The aim is to fully isolate the effects of uniform B_x and B_z on the near wall flow in order to understand how they coact with the fine structure of the turbulence. As the wall normal B_y field interacts directly with the mean flow and consequently leads to undesirable magnetic brake effects, it is not examined here.

A. Pressure gradient and drag reduction

In the case of the wall normal magnetic field B_y , the streamwise Reynolds averaged Navier-Stokes equation contains a mean Lorentz force. The mean velocity is directly affected by B_y . The B_y effect on turbulent drag results from the competition between the drag increase due to the thin Hartmann layer near the wall and the skin friction decrease due to the turbulence suppression. The Hartmann effect dominates the drag at large Stuart numbers, resulting in a drag increase. On the other hand, the skin friction decreases at small N_τ because of the predominance of turbulence suppression. In the wall-parallel magnetic field cases, thus, the drag always decreases due to the turbulence suppression [6,21,22].

Figure 2 shows the evolution of the viscous drag as a function of the Stuart number. The volume-averaged Lorentz force is assumed to be zero because the global condition $\iiint_V \mathbf{j} dx dy dz = 0$ is maintained. The longitudinal mean pressure gradient term is for each time step deduced from the integration of the viscous shear stress on the walls. Note that the mean pressure gradient $-(\frac{\partial P}{\partial x})$ in Fig. 2 directly provides the drag reduction. The drag decreases with the Hartmann number, and the flow reaches a relaminarized state at a value of $N_\tau \approx 0.11$ ($Ha = 60$) for a streamwise magnetic field. The flow is relaminarized at a significantly lower Stuart number $N_\tau = 7 \times 10^{-3}$ ($Ha = 15$) under the spanwise magnetic field B_z compared to B_x . Therefore, imposing a transverse magnetic field is undeniably more efficient than imposing B_x in terms of drag reduction.

B. Mean velocity and turbulent shear stresses

The mean streamwise velocity profiles U_x are shown in Fig. 3 for both streamwise and spanwise magnetic field orientation. It is seen that, up to the relaminarization, U_x is only moderately altered by B_x [Fig. 3(a)] and B_z [Fig. 3(b)]. However, once a magnetic intensity threshold is exceeded, the flow is suddenly relaminarized and U_x coincides subsequently with the Poiseuille profile. These thresholds depend on the magnetic field orientation, and they are $N_\tau = 0.11$ ($Ha = 60$) and $N_\tau = 7 \times 10^{-3}$ ($Ha = 15$) for the streamwise and spanwise oriented magnetic fields, respectively.

Figure 4(a) shows a visible increase of the turbulent activity associated with the streamwise velocity fluctuations with N_τ before relaminarization. Additional investigations (not shown here) have revealed that the time- and volume-averaged rms of the streamwise velocity fluctuations increased by up to 40% in the range $0 < N_\tau < 0.09$ ($0 < Ha < 55$), prior to its sharp decline. This

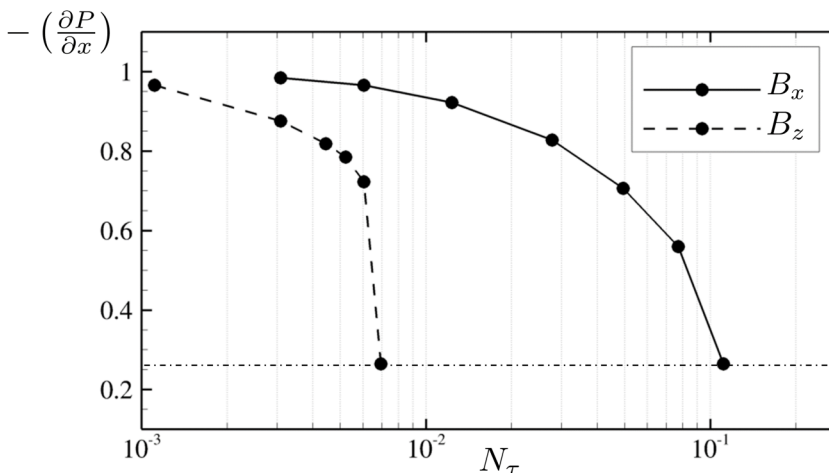


FIG. 2. Evolution of streamwise pressure loss for various streamwise and spanwise magnetic field intensities. The mean pressure gradient $-\left(\frac{\partial P}{\partial x}\right)$ is nondimensionalized by the unmanipulated turbulent channel flow counterpart. The dotted-dashed line represents the laminar limit.

behavior has been discussed in detail in the literature. It has been tentatively linked to the transfer from small to large scales in the outer region, and to the observation that the magnetic field increases the scale of streamwise energy containing eddies [6,22]. It can be also noted that streamwise velocity fluctuations are not completely damped in the inner region at $N_\tau = 0.11$ ($Ha = 60$) as also observed by Tsinober [23]. It is interesting to note that in the near wall region the rms of the streamwise velocity fluctuations u'_x is only faintly altered up to the relaminarization in the low buffer layer $y < 15$. We recall that the rms of a quantity q is here denoted by q' and defined by $q' = \sqrt{\overline{q \cdot q}}$. The wall normal component u'_y [Fig. 4(b)] and the spanwise turbulent intensity u'_z [Fig. 4(c)] together with the Reynolds shear stress [Fig. 4(d)] are, however, more gradually affected by B_x .

Figure 5 shows that in the low buffer layer ($y < 15$) the Reynolds shear-stress and fluctuating velocities are only slightly altered under the effect of the spanwise magnetic field B_z . This is particularly the case for the fluctuating streamwise component [Fig. 5(a)], which evolves identically in the full depth of the channel until a sudden decrease around $N_\tau = 7 \times 10^{-3}$ ($Ha = 15$) leads to the relaminarized state.

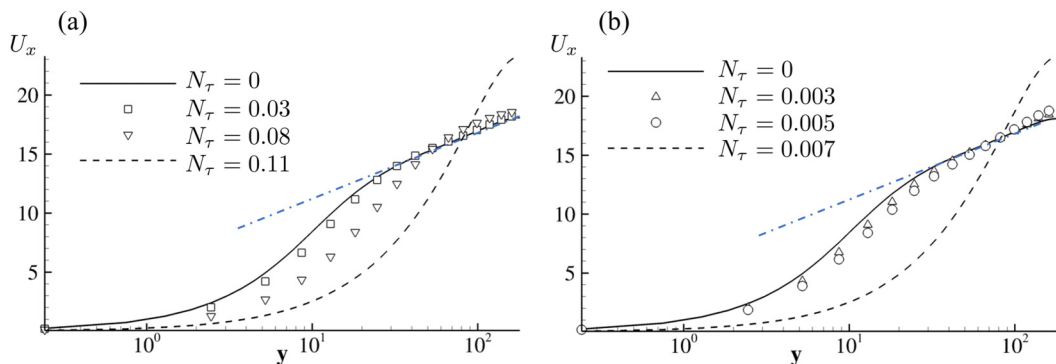


FIG. 3. Effect of the Hartmann number on the mean streamwise velocity profile U_x . (a) Streamwise uniform magnetic field B_x . (b) Spanwise uniform magnetic field B_z . Standard log-law profile ($2.5 \ln y + 5.5$) of the canonical turbulent channel flow is represented by the blue dashed-dot line.

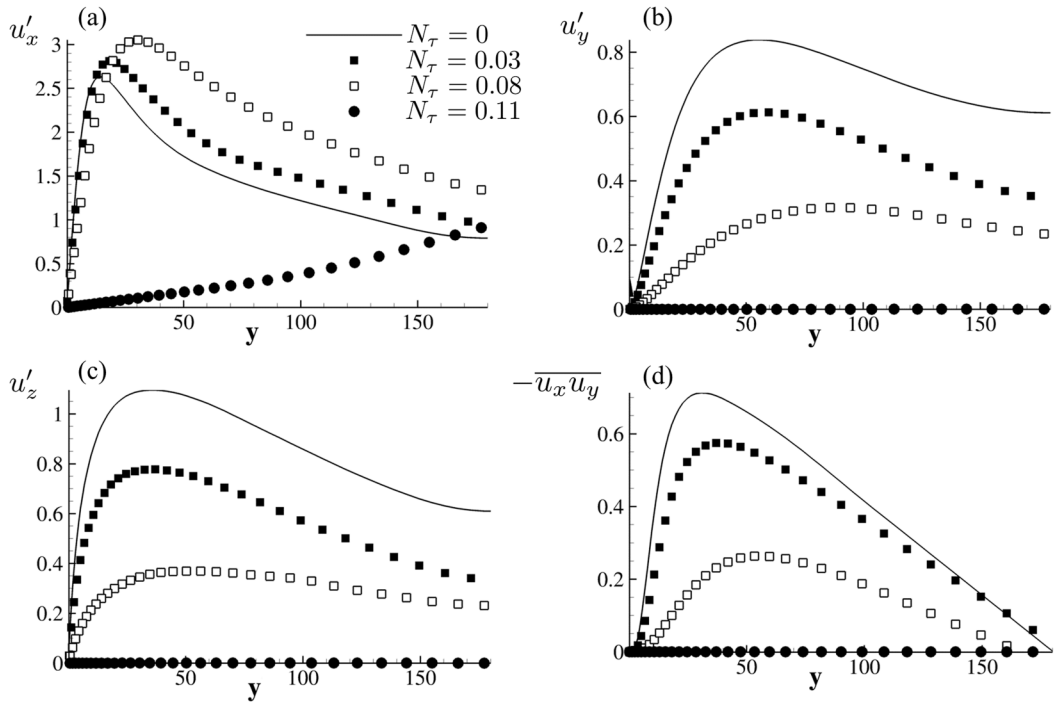


FIG. 4. Effect of the streamwise magnetic field on (a) streamwise, (b) wall-normal, (c) and spanwise turbulent activities and (d) Reynolds shear stress.

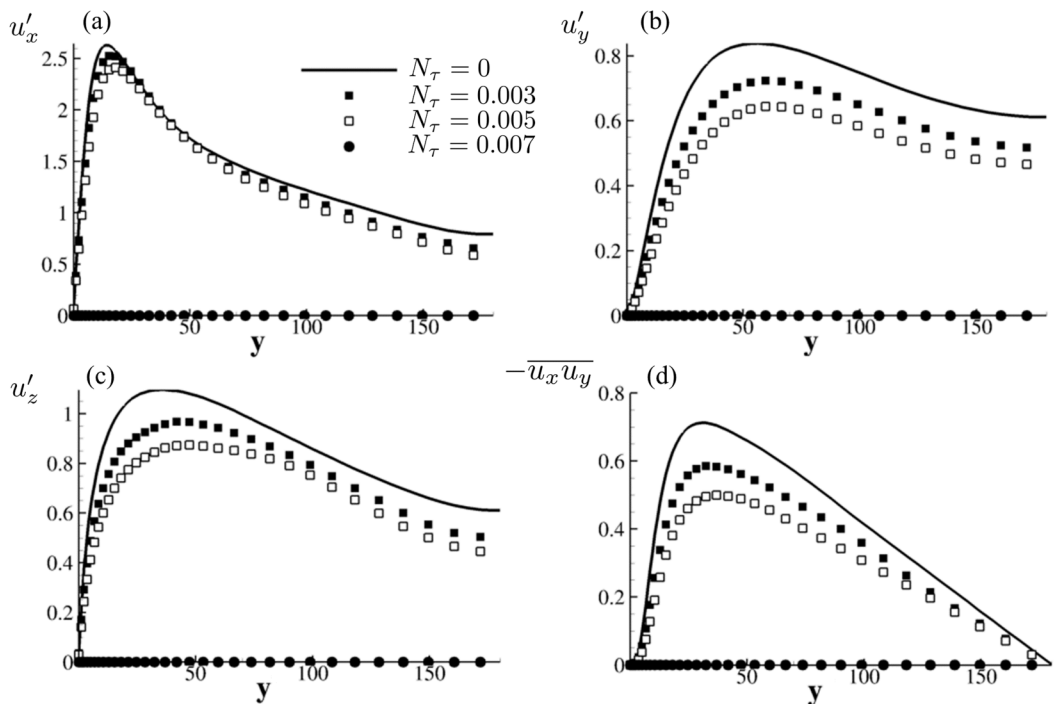


FIG. 5. Same as Fig. 4 but in the case of the spanwise magnetic field.

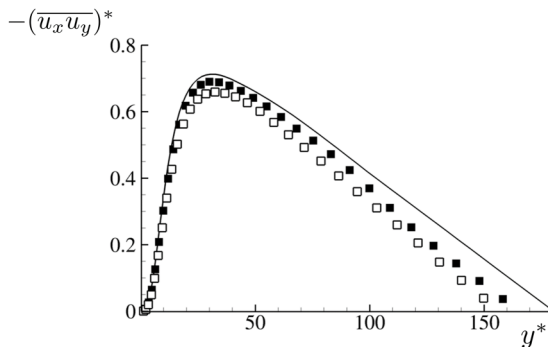


FIG. 6. Same results as Fig. 5(d), but the quantities are now scaled by the local shear velocity and the viscosity. See text for details.

It is important to emphasize one point albeit briefly, without showing the corresponding results. One of the main characteristics of drag reduction in wall turbulence is the relative insensitivity of the turbulent intensities when they are scaled with the local shear velocity $u_\tau = \sqrt{\tau_w/\rho}$ where τ_w is the local wall shear stress (and not that of the unmanipulated flow). This is a more or less universal feature of wall turbulence, independent of the drag reducing mechanism [14]. Denoting these scaled rms quantities by $u_i'^*$, it is found here that $u_i'^*$ profiles collapse more or less independently of the Stuart number N_τ under both the streamwise and spanwise magnetic field. Figure 6 shows, for instance, the $-\overline{u_x u_y}^*$ versus y^* profiles for the spanwise magnetic field. There is an acceptably good collapse of these profiles, especially in the inner layer.

Lee and Choi [6] have shown that the Lorentz force-induced term in the local streamwise vorticity transport equation is negatively correlated with the $\frac{\partial u_y}{\partial z}$ component of ω_x , and as a result is weakened by B_z . Krasnov *et al.* [21] have also confirmed that the main effect of a transverse magnetic field is the suppression of momentum transfer in the wall-normal direction. Such effects are absent in the B_x case.

C. Electric current field

Figure 7 shows the rms distributions of the electric current field under B_x and B_z at $N_\tau = 6 \times 10^{-3}$ ($Ha = 14$). Remember that there is no interaction between the magnetic field and the streamwise mean velocity, and that there is no mean electric current involved. Thus, the statistics of the electric current fluctuations depend only slightly on N_τ . We carefully checked this point by analyzing the current field intensities at different Stuart numbers (not shown here). The turbulent current fields are significantly more intense under the spanwise than the streamwise magnetic field (Fig. 7). It is found for the B_z case that j_y' , and j_x' peak in the neighborhood of the buffer layer, at $y = 30$ and $y = 45$, respectively, while the maximum in j_z' is at the wall $y = 0$. Thus, there is no clear local maxima in the j' distributions under the streamwise magnetic field.

In order to gain further insight into the electric current field, we decomposed j into two components according to $\mathbf{j} = -\nabla\phi + \mathbf{u} \times \mathbf{B}$. Thus, the electric field is decomposed into a conductive $\mathbf{j}_c = -\nabla\phi$ and an electromotive $\mathbf{j}_{em} = \mathbf{u} \times \mathbf{B}$ part. Figure 8 shows the rms of these components for j_y and j_z . For the sake of brevity, we do not present the j_x profiles because the magnitudes of the corresponding components $j'_{c,x}$ and $j'_{em,x}$ are comparably small. The first striking result emerging from Fig. 8 is the emancipation of clear local maxima in j'_c and j'_{em} situated in the middle buffer layer or slightly above. Consider for instance Fig. 8(b) corresponding to the spanwise magnetic case. First, note that j_z is purely conductive and that consequently $j'_{em,z} = 0$. Second, the peaks in $j'_{em,y}$ and $j'_{c,y}$ of the wall normal current are situated at $y \approx 20$ in the middle of the buffer layer. The local maxima of $j'_{em,y}$ and $j'_{c,y}$ under B_x in Fig. 8(a) are also positioned near the same location. It is well known that

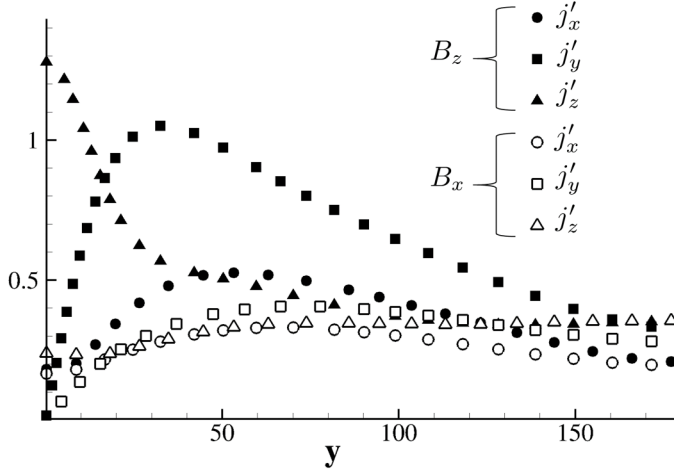


FIG. 7. Distribution of the electric current fluctuating intensities for B_x (white symbols) and B_z (black symbols). Circles: j'_x ; squares: j'_y ; triangles: j'_z . $N_\tau = 6 \times 10^{-3}$ ($Ha = 14$).

the coherent shear stress producing eddies largely populate the buffer layer, and their impact on the self-organisation of the conductive and electromotive current fields is undeniable. We will discuss these points in Sec. IV. Last, it is interesting to note from Fig. 8 that the rms of the electromotive and conductive components are twice as large than j' . Noting simply that $j'^2 = j_c'^2 + j_{em}'^2 + \overline{j_c j_{em}}$ leads to $\overline{j_c j_{em}} < 0$, that is, the fluctuating electromotive current is negatively correlated with the conductive current. This is consistent with the electric field induced by the coherent quasistreamwise buffer layer vortices, as will also be discussed in Sec. IV. There is no doubt that the decomposition $\mathbf{j} = \mathbf{j}_c + \mathbf{j}_{em}$ is a prime necessity to sort out these characteristics.

D. Shear stresses transport

The key elements that explain the rapid relaminarization under the transverse magnetic field are intrinsically related to the transport process of the turbulent shear stresses. The mean transport equation of the Reynolds shear stress tensor $u_i u_j$ under a uniform magnetic field can be

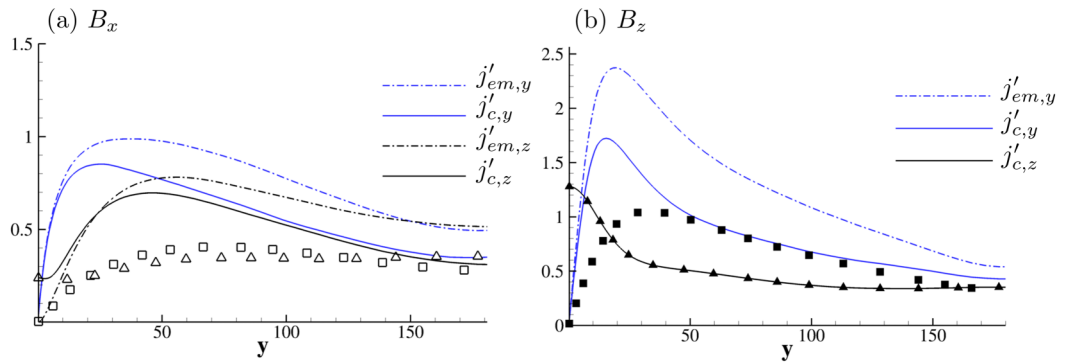


FIG. 8. RMS of electromotive and conductive electric currents contributions under (a) a longitudinal or (b) a spanwise magnetic field ($N_\tau = 6 \times 10^{-3}$). Same symbols as legend in Fig. 7. Blue lines: wall-normal currents (on y direction); black lines: spanwise currents (on z). Solid lines: conductive currents j_c ; dash-dotted lines: electromotive currents j_{em} .

expressed as

$$\frac{\mathcal{D}\overline{u_i u_j}}{\mathcal{D}t} = \mathcal{P}_{ij} + T_{ij} + \pi_{ij}^{(s)} + \pi_{ij}^{(d)} + \mathcal{D}_{ij} + \varepsilon_{ij} + \mathcal{M}_{ij}. \quad (7)$$

The production, turbulent diffusion, pressure strain, pressure diffusion, molecular diffusion, and dissipation terms appearing on the right-hand side are

$$\begin{aligned} \mathcal{P}_{ij} &= -\overline{u_j u_k} \frac{\partial U_i}{x_k} - \overline{u_i u_k} \frac{\partial U_j}{x_k}, & T_{ij} &= -\frac{\partial \overline{u_i u_j u_k}}{\partial x_k}, \\ \pi_{ij}^{(s)} &= p \left(\frac{\partial u_j}{\partial x_i} + \frac{\partial u_i}{\partial x_j} \right), & \pi_{ij}^{(d)} &= -\left(\frac{\partial \overline{p u_j}}{\partial x_i} + \frac{\partial \overline{p u_i}}{\partial x_j} \right), \\ \mathcal{D}_{ij} &= \frac{\partial^2 \overline{u_i u_j}}{\partial x_l \partial x_l}, & \varepsilon_{ij} &= -2 \left(\frac{\partial \overline{u_i}}{\partial x_l} \frac{\partial u_j}{\partial x_l} \right). \end{aligned} \quad (8)$$

The term directly related to the magnetic field is

$$\mathcal{M}_{ij} = N_\tau (\epsilon_{jkl} \overline{u_i j k} \cdot B_l + \epsilon_{ilk} \overline{u_j j l} \cdot B_k) \quad (9)$$

where

$$\overline{u_i j_i} = -u_i \frac{\partial \phi}{\partial x_i} + \overline{u_i \epsilon_{ijk} u_j B_k} \quad (10)$$

and ϵ_{ijk} is the Levi-Civita operator. Hereafter, the subindices 1, 2, and 3 will directly be replaced by the corresponding directions z , y , and x , respectively, in order to alleviate the notations and facilitate the reading. For example, the production in the $\frac{\mathcal{D}\overline{u_x u_x}}{\mathcal{D}t}$ transport equation will be denoted by \mathcal{P}_{xx} . Remember that the quantities are scaled here with respect to the shear velocity of the unmanipulated turbulent channel flow and the kinematic viscosity. Thus, the Stuart number appearing in \mathcal{M}_{ij} is given by $N_\tau = (\text{Ha}/\text{Re}_\tau)^2$. The MHD induced terms can be further decomposed into a source (S) and annihilation (A) component. Hereafter, this decomposition is denoted by $\mathcal{M}_{ij} = S_{ij}^{St} + A_{ij}^{St}$ for the streamwise magnetic field and $\mathcal{M}_{ij} = S_{ij}^{Sp} + A_{ij}^{Sp}$ for the spanwise one. The uniform streamwise magnetic field corresponds to $B_y = B_z = 0$, resulting in the following:

- (1) M_{zz} : $S_{zz}^{St} = 2N_\tau \overline{(u_x \frac{\partial \phi}{\partial y})}$ and $A_{zz}^{St} = -2N_\tau \overline{u_x u_z}$
- (2) M_{yy} : $S_{yy}^{St} = 2N_\tau \overline{(u_y \frac{\partial \phi}{\partial z})}$ and $A_{yy}^{St} = -2N_\tau \overline{u_y u_y}$
- (3) M_{xx} : $S_{xx}^{St} = 0$ and $A_{xx}^{St} = 0$
- (4) M_{xy} : $S_{xy}^{St} = N_\tau \overline{(u_x \frac{\partial \phi}{\partial z})}$ and $A_{xy}^{St} = -N_\tau \overline{u_x u_y}$.

The spanwise magnetic field with $B_x = B_y = 0$ leads to

- (1) M_{zz} : $S_{zz}^{Sp} = 0$ and $A_{zz}^{Sp} = 0$
- (2) M_{yy} : $S_{yy}^{Sp} = -2N_\tau \overline{(u_y \frac{\partial \phi}{\partial x})}$ and $A_{yy}^{Sp} = -2N_\tau \overline{u_y u_y}$
- (3) M_{xx} : $S_{xx}^{Sp} = 2N_\tau \overline{(u_x \frac{\partial \phi}{\partial y})}$ and $A_{xx}^{Sp} = -2N_\tau \overline{u_x u_x}$
- (4) M_{xy} : $S_{xy}^{Sp} = N_\tau \overline{(u_y \frac{\partial \phi}{\partial y} - u_x \frac{\partial \phi}{\partial x})}$ and $A_{xy}^{Sp} = -2N_\tau \overline{u_x u_y}$

corresponding to $N_\tau = 6 \times 10^{-3}$ ($\text{Ha} = 14$). This corresponds to the situation just before the flow is relaminarized under the spanwise magnetic field (Fig. 2). First, consider the transport of the Reynolds shear stress tensor ($\overline{u_x u_y} < 0$) under the streamwise magnetic field B_x . It is obvious that $A_{xy}^{St} = -N_\tau \overline{(u_x u_y)}$ is a destruction term, since it is opposite in sign to $\overline{u_x u_y} < 0$. We find out, thus, that $S_{xy}^{St} = N_\tau \overline{(u_x \frac{\partial \phi}{\partial z})}$ is always negative in all the cases investigated here. This term constitutes therefore a source term in the $\frac{\mathcal{D}\overline{u_x u_y}}{\mathcal{D}t}$ equation. Figure 9(c) shows the distributions of these quantities. For comparison, the production term $\mathcal{P}_{xy} = -2\overline{u_y u_y} \frac{\partial U_x}{\partial y}$ is also shown in Fig. 9(c) (right-hand blue scale).

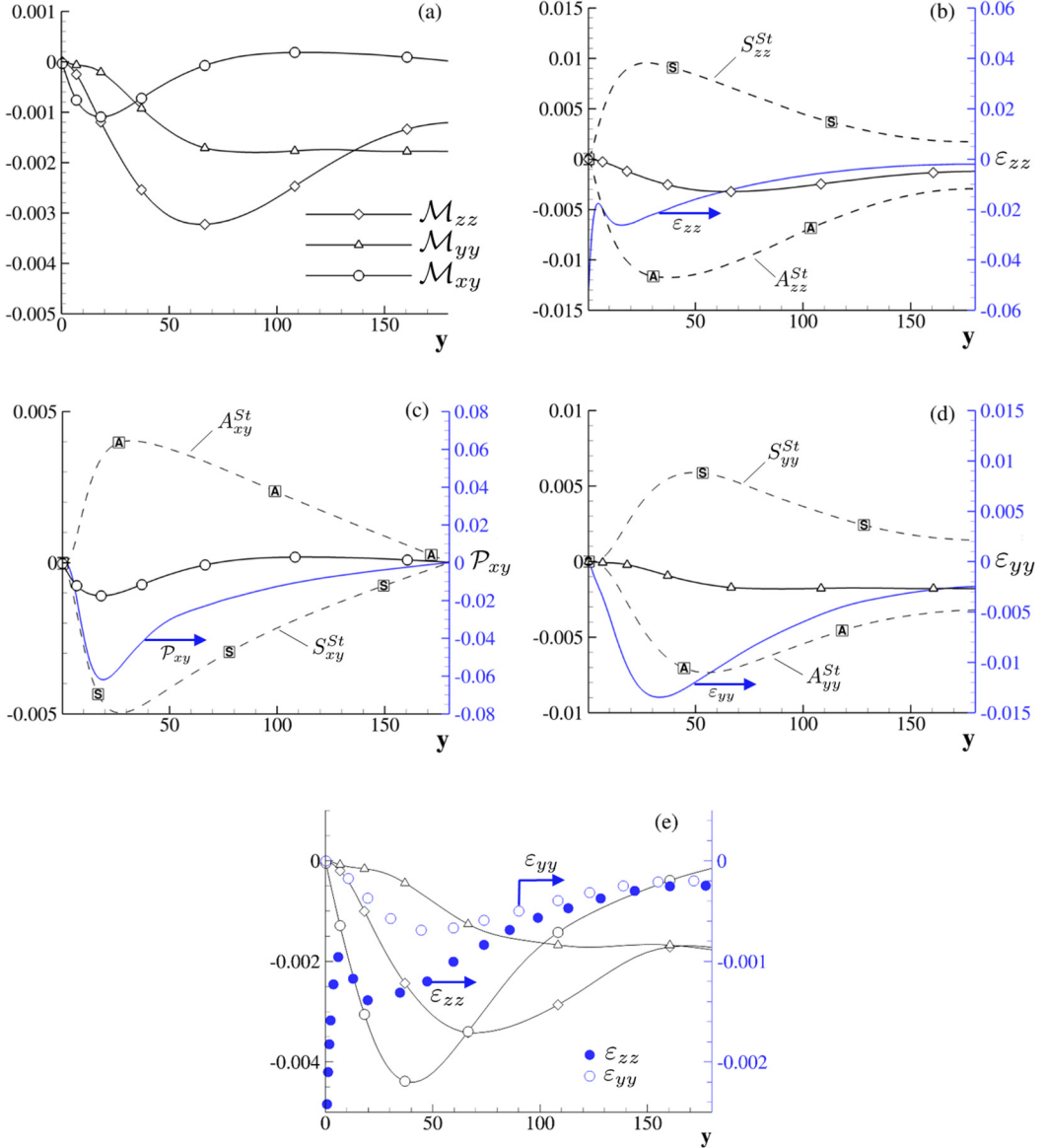


FIG. 9. $N_\tau = 6 \times 10^{-3}$ ($Ha = 14$). (a) MHD transport terms \mathcal{M}_{ij} under longitudinal B_x . (b) \mathcal{M}_{zz} (plain line with symbol), S-dashed line: S_{zz}^{St} , A-dashed line: A_{zz}^{St} , blue line: dissipation ε_{zz} . (c) \mathcal{M}_{xy} (plain line with symbol), S-dashed line: S_{xy}^{St} , A-dashed line: A_{xy}^{St} , blue line: production \mathcal{P}_{xy} . (d) \mathcal{M}_{yy} (plain line with symbol), S-dashed line: S_{yy}^{St} , A-dashed line: A_{yy}^{St} , blue line: dissipation ε_{yy} . (e) MHD transport terms \mathcal{M}_{ij} under streamwise B_x for $N_\tau = 0.08$ ($Ha = 50$) and dissipation terms ε_{yy} (empty blue circles) and ε_{zz} (plain blue circles).

It is interesting to note that there is an equilibrium in a rough sense between S_{xy}^{St} and $-A_{xy}^{St}$ in the whole layer and particularly at $y > 50$. Thus, the net contribution of the direct streamwise MHD effect to the shear stress transport is almost zero [Figs. 9(a) and 9(c)]. The negative peak appearing in \mathcal{M}_{xy} in the buffer layer is an order of magnitude smaller than \mathcal{P}_{xy} and is entirely negligible, as are the individual source and destruction terms that are an order of magnitude smaller than \mathcal{P}_{xy} [Fig. 9(c)]. This means that the direct contribution of the imposed B_x is insignificant on the Reynolds shear stress transport.

The net contribution of \mathcal{M}_{zz}^{St} to the spanwise turbulent velocity intensity transport $\frac{D\overline{u_z u_z}}{Dt}$ under B_x is also small as seen in Fig. 9(b). Note that, since the production term is $\mathcal{P}_{zz} = 0$, the MHD source and destruction terms S_{zz}^{St} and A_{zz}^{St} are compared to the dissipation ε_{zz} in Fig. 9(b). It is interesting to note that individually, both S_{zz}^{St} and A_{zz}^{St} are far from being negligible and reach values as large as $\varepsilon_{zz}/2$, particularly at the edge of the buffer layer. However, the balance is such between the MHD source and annihilation terms that their sum ends up being insignificant. The S_{yy}^{St} and A_{yy}^{St} terms appearing in the normal velocity intensity transport equation $\frac{D\overline{u_y u_y}}{Dt}$ under B_x shown in Fig. 9(d) are also not negligible when viewed individually, and are even comparable with the dissipation. Note, for instance, that $S_{yy}^{St} \approx \varepsilon_{yy}/2$ at $y > 50$. But the net effect \mathcal{M}_{yy}^{St} is still irrelevant compared to ε_{yy} . Hence, in the case of a streamwise magnetic field, the MHD contributions to the transport equations and the flow organization are found to be individually strong but collectively negligible at this particular Stuart number. Note in Fig. 9(a) that \mathcal{M}_{yy}^{St} and \mathcal{M}_{zz}^{St} are negative; that is, the destruction overcomes the sources terms in the related transport equations. The net destruction effects over $\overline{u_y u_y}$ and $\overline{u_z u_z}$ increase with N_τ . However, an order-of-magnitude larger Stuart number of approximately $N_\tau > 6 \times 10^{-2}$ is necessary, so that \mathcal{M}_{yy}^{St} and \mathcal{M}_{zz}^{St} can be compared to the related dissipation terms ε_{yy} and ε_{zz} .

Figure 9(e) recapitulates the MHD transport terms \mathcal{M}^{St} at $N_\tau = 0.08$ ($Ha = 50$) before the relaminarization under B_x (Fig. 2). It is seen that \mathcal{M}_{xy}^{St} stays negative. Therefore, the direct effect of the streamwise magnetic field on $(\overline{u_x u_y})$ becomes even enhancing at this large Stuart number. But the terms \mathcal{M}_{yy}^{St} and \mathcal{M}_{zz}^{St} exceed the dissipation terms ε_{yy} and ε_{zz} by a factor larger than three above the buffer layer. Thus, the wall normal and spanwise velocity fluctuations are now strongly weakened by the magnetic field. There is an indirect subsequent effect on the Reynolds shear stress that also consequently decreases [Fig. 4(d)]. To resume, the primary B_x effect is the damping of the wall normal and spanwise turbulent activity, with a feedback on the Reynolds shear stress. This is a slow process in terms of turbulent drag reduction.

The situation is entirely different under the uniform spanwise magnetic field B_z . The destruction and source terms in the Reynolds shear stress transport equation are now $A_{xy}^{Sp} = 2N_\tau(-\overline{u_x u_y})$ and $S_{xy}^{Sp} = N_\tau(u_y \frac{\partial \phi}{\partial y} - u_x \frac{\partial \phi}{\partial x})$, respectively. Note that A_{xy}^{Sp} is twice as large in B_z than B_x ($A_{xy}^{St} = N_\tau(-\overline{u_x u_y})$). More interestingly, it is found here that the source term is $S_{xy}^{Sp} \ll A_{xy}^{Sp}$, independent of N_τ . Figure 10(c) compares the A_{xy}^{Sp} and S_{xy}^{Sp} profiles directly with the production \mathcal{P}_{xy} . It can be clearly seen that S_{xy}^{Sp} is nearly an order of magnitude smaller than $-A_{xy}^{Sp}$. This leads to a net MHD destruction $\mathcal{M}_{xy}^{Sp} > 0$, which becomes substantial [Fig. 10(a)]. In addition, the destruction term A_{xy}^{Sp} reaches values as large as $\frac{1}{4}\mathcal{P}_{xy}$ at $y > 50$ as can clearly be seen in Fig. 10(c).

It would therefore be interesting at this stage to estimate the value of the interaction parameter required to entirely annihilate the production $\mathcal{P}_{xy} = -2\overline{u_y u_y} \frac{\partial U_x}{\partial y}$ at the edge of the buffer layer. It has been indicated before that the turbulent quantities scaled by the local shear stress velocity and the viscosity are more or less invariant with N_τ and compare with the unmanipulated channel flow in a rough sense. Thus, equilibrating the MHD destruction and production terms results in $\mathcal{P}_{xy}^* = -2N_\tau(\overline{u_x u_y}^*)$ where (*) stands for the quantities scaled by the local $\overline{u_\tau}$. One has here $\mathcal{P}_{xy}^* = 0.05$ and $-\overline{u_x u_y}^* = 0.7$ at $y = 30$, in agreement with Mansour and Moin [24]. This estimation leads to $N_\tau \approx 0.02$ ($Ha \approx 30$). Thus, at $N_\tau \approx 0.02$, the net MHD destruction would be larger than the shear stress production in the logarithmic and the outer layer. The sudden relaminarization under B_z takes place at $N_\tau = 0.006$ ($Ha = 15$), which is three times smaller than the estimated value (Fig. 2). Yet this rough estimation is quite fair, considering that B_z severely reduces the turbulent activity in a large part of the turbulent layer. Furthermore, as Re_τ becomes large enough, $-\overline{u_x u_y}^* \rightarrow 1$, in the logarithmic layer extending into a large region delimited by $3\sqrt{Re_\tau} < y^* < 0.15Re_\tau$ [25]. The shear decreases as $\frac{\partial U_x^*}{\partial y^*} \propto \frac{1}{\kappa y^*}$ in the log layer, where κ is the von Kármán constant, while $\overline{u_y u_y}^*$ is insensitive to Re_τ , in a rough sense, according to the Townsend attached eddy hypothesis [26]. This implies that the direct MHD destruction may possibly be more competitive in terms of contracting

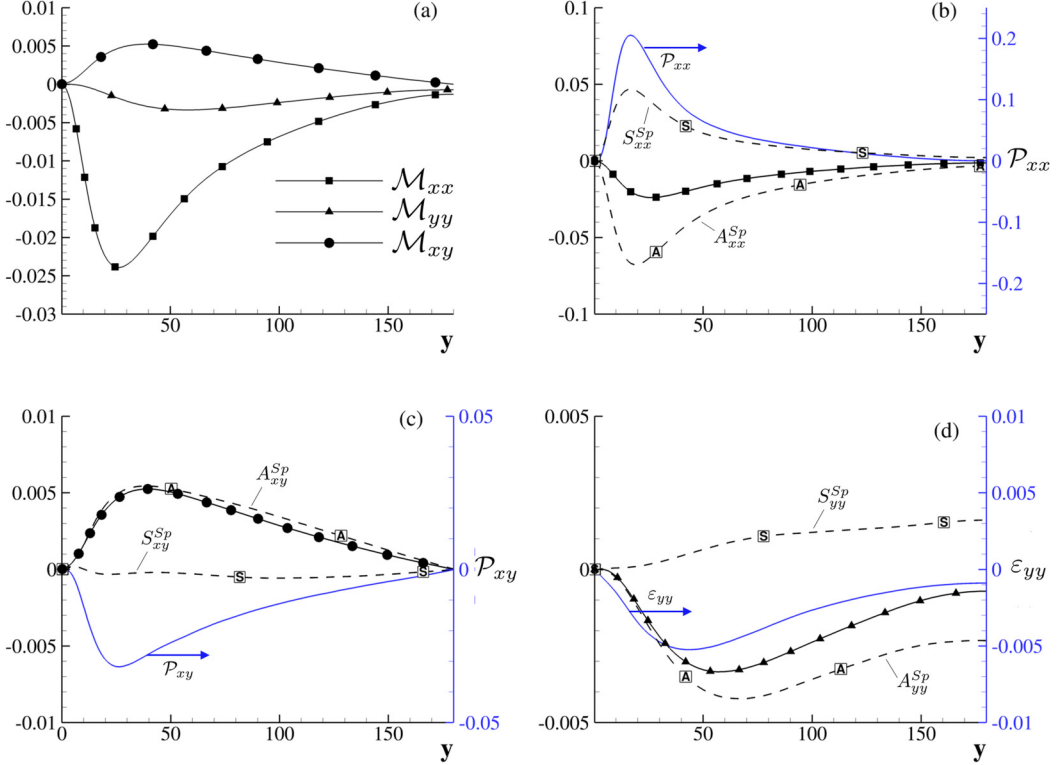


FIG. 10. $N_\tau = 6 \times 10^{-3}$ ($Ha = 14$). (a) MHD Transport terms \mathcal{M}_{ij} under transverse B_z . (b) \mathcal{M}_{xx} (plain line with symbol), S-dashed line: S_{xx}^{Sp} , A-dashed line: A_{xx}^{Sp} , blue line: production \mathcal{P}_{xx} . (c) \mathcal{M}_{xy} (plain line with symbol), S-dashed line: S_{xy}^{Sp} , A-dashed line: A_{xy}^{Sp} , blue line: production \mathcal{P}_{xy} . (d) \mathcal{M}_{yy} (plain line with symbol), S-dashed line: S_{yy}^{Sp} , A-dashed line: A_{yy}^{Sp} , blue line: dissipation ε_{yy} .

the production \mathcal{P}_{xy}^* at large Reynolds numbers Re_τ , wherein the log layer extends over a large range of y^* . The fact still remains that there is a net Reynolds shear stress destruction effect induced by the uniform spanwise magnetic field. Furthermore, the direct contribution of the turbulence to the friction coefficient in the canonical turbulent channel flow is a weighted integral of the distribution of the Reynolds shear stress across the channel [27]. Indeed, the original FIK decomposition [27] is directly applicable here, because the mean momentum equation is formally identical to that of the unmanipulated channel flow. The turbulent part of the skin friction coefficient denoted by C_{ft} and scaled by the bulk velocity is exactly $C_{ft} = 6 \int_0^1 (1 - y_*) (-\overline{u_x u_y})_* dy_*$, where $(\cdot)_*$ denotes the quantities scaled by the outer variables based on the bulk velocity and the channel half-width. This relation shows that B_z acts on turbulent drag by modifying progressively the Reynolds shear stress through the whole channel, as N_τ increases. For all these reasons, the relaminarization under B_z requires smaller Stuart number than B_x .

The resultant \mathcal{M}_{xx}^{Sp} in the streamwise velocity transport $\frac{D\overline{u_x u_x}}{Dt}$ is negligible. Indeed, \mathcal{M}_{xx}^{Sp} is an order of magnitude smaller than the production \mathcal{P}_{xx} near the wall [Fig. 10(b)]. Nonetheless, the direct effect of the spanwise magnetic field on the wall normal turbulent velocity intensity transport $\frac{D\overline{u_y u_y}}{Dt}$ is substantial. The destruction term $A_{yy}^{Sp} = -2N_\tau (\overline{u_y u_y})$ largely overcomes the MHD source term S_{yy}^{Sp} in Fig. 10(a). It can be clearly seen in Fig. 10(d) that the effect of the resulting \mathcal{M}_{yy}^{Sp} is relentless and that \mathcal{M}_{yy}^{Sp} is directly comparable to the dissipation ε_{yy} in the whole layer. Therefore, the spanwise magnetic field significantly dumps the wall normal turbulence activity, and this by

direct MHD effects. Overall the imposed B_z interacts with the Reynolds shear stress transport phenomena, and it is subsequently more efficient in terms of drag reduction compared to B_x . This interaction is a result of the precise reorganization of the flow field induced by the magnetic field, near and around the near wall coherent eddies. Indeed, the results presented in this section can hardly be interpreted through simple considerations concerning the correlations between the fluctuating velocity field and the Lorentz force [6]. The role of the near wall coherent structures is crucial as will be discussed in the next section.

IV. TURBULENT STRUCTURES AND CONDITIONAL AVERAGING

A. Coherent structures identification

Coherent structures play a fundamentally important role in the transport of momentum and scalar quantities (see Tardu [28] for a review). Curiously enough, the contribution of the Reynolds shear stress producing eddies to the generation of the current field, and to the direct MHD-induced terms in the shear stress transport equations, has not yet been investigated to our best knowledge. This should therefore be an important point to consider, especially with respect to the analysis of the fluctuating current field. As we highlighted before, the rms distributions of the latter, once decomposed into electromotive and conductive parts, present clear local peaks in or near the buffer layer (Fig. 8). This is all the more reason to investigate the specific MHD flow elements induced by the coherent quasistreamwise vortices.

The quasistreamwise vortices (QSVs) are detected with the classical λ_2 technique introduced by Jeong and Hussain [29]. The parameter λ_2 is the second largest negative eigenvalue of the tensor $S_{ik}S_{kj} + \Omega_{ik}\Omega_{jk}$, where $S_{ij} = (u_{i,j} + u_{j,i})/2$ and $\Omega_{ij} = (u_{i,j} - u_{j,i})/2$ are the symmetric and antisymmetric parts of the velocity gradient tensor $u_{i,j} = \frac{\partial u_i}{\partial x_j}$. The conditional averages are performed in a way similar to Jeong *et al.* [30]. In short, the local maxima of $-\lambda_2$, with either positive or negative streamwise vorticity ω_x are determined in the homogeneous planes, and the line connecting these maxima is attributed to the vortex axis. Structures with inclination and tilting angles of $\pm 30^\circ$, whose centers are located at $y \geq 10$, and extending at least 110 wall units in the streamwise direction are selected. Each individual structure is aligned into a subdomain of dimensions $n_z \times n_y \times n_x = 110 \times 80 \times 350$ wall units. The median plane P_0 of the conditional structure is subsequently unambiguously determined. The conditional averages are performed using 25 statistically independent snapshots separated in time by $100h/U_{cp}$. All in all, more than 100 structures with either positive or negative streamwise vorticity were selected to perform the conditional averages. We present only the results emerging from the educed structures with positive streamwise vorticity $\omega_x > 0$, the extension of the results for structures with $\omega_x < 0$ being straightforward. Hereafter, the conditional average of a quantity q is denoted by $\langle q \rangle$. Figure 11(a) shows the streamlines associated to the conditional structure educed from this process. The median plane P_0 is also shown in this figure. The length and the diameter of the structure are 170 and 20 wall units, respectively. The conditional positive and negative streamwise velocity contours in the plane P_0 are shown in Fig. 11(b). Figure 11(c) shows the relative locations of the quadrant events, i.e., Q_1 ($u_x > 0, u_y > 0$), Q_2 (or ejections, $u_x < 0, u_y > 0$), Q_3 ($u_x < 0, u_y < 0$), and Q_4 (or sweeps, $u_x > 0, u_y < 0$) with respect to the conditional structure. Figure 11 is both qualitatively and quantitatively in agreement with Jeong *et al.* [30] (their Fig. 13).

B. Conditional averages and discussion

The conditional averages in the P_0 plane of the source and annihilation terms, constituting \mathcal{M}_{ij} [Eq. (9)] are shown in Figs. 12 and 16, for the streamwise and spanwise magnetic fields, respectively.

Figure 12 shows that the source and annihilation sites coincide quasiperfectly around the quasistreamwise vortices under B_x . Furthermore, the intensities of $\langle S_{ij}^{St} \rangle$ compare quite well with $\langle A_{ij}^{St} \rangle$, pointing at a quasiequilibrium between the MHD source and destruction effects at this

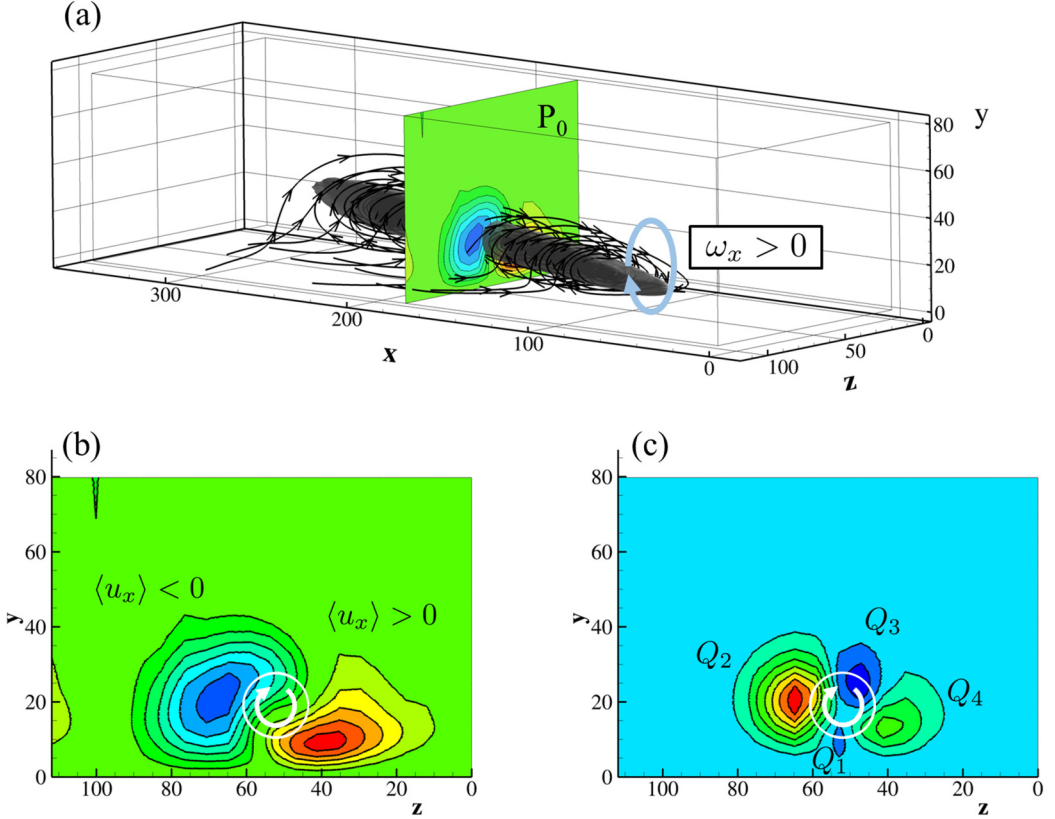


FIG. 11. Conditionally averaged QSV ($\omega_x > 0$) in case of a unmanipulated turbulent channel flow, (i.e., without magnetic field) for $Re_\tau = 180$. (a) Fluctuation-based streamlines and location of the midplane P_0 ; (b) streamwise fluctuating contours $\langle u_x \rangle$ in P_0 (Min = -3.5 ; Max = 2.5 ; Step = 0.5); (c) coherent Reynolds stress contours $-\langle u_x u_y \rangle$ in P_0 (Min = -1 ; Max = 3 ; Step = 0.5).

particular Stuart number. The streamwise magnetic field significantly affects the individual source and destruction terms in the wall normal and spanwise velocity fluctuations transport equations. Yet, for example, the global B_x effect remains weak at $N_\tau = 6 \times 10^{-3}$ (Fig. 9). The rms peak values of the electromotive and conductive current profiles [Fig. 8(a)] are intimately connected to the interaction between the imposed magnetic and the coherent velocity fields. Figure 13 shows the conditional averages of electromotive j_{em} and conductive j_c distributions in the P_0 plane under B_x . It is clearly seen that the generation of the electromotive current in the wall normal direction y [Fig. 13(a)] or along the spanwise direction z [Fig. 13(b)] induces a conductive current field of opposite sign and of almost equivalent intensity. This is schematically shown in Fig. 13(c). From this last figure, it is now relatively easy to understand the role played by the conditional averages of the direct source and annihilation terms in the Reynolds shear stress transport equation. The electric current field shown in Fig. 13(c) indeed explains why the term $\langle S_{xy}^{Sr} \rangle = N_\tau \langle u_x \frac{\partial \phi}{\partial z} \rangle$ is negative, and why it is therefore an MHD source term. The quasistreamwise vortex with positive streamwise vorticity shown in Fig. 13(c) induces a wall normal velocity $u_y < 0$ site, at the sweep right-hand side of the structure. The $u_y < 0$ zone produces a negative electromotive current field $j_{em,z} < 0$ through $\mathbf{u} \times \mathbf{B}$. This is shown by the orange arrows. Reasoning in the same way for all coherent events implies that the current field is centrifugal.

Now, since $\text{div}(\mathbf{j}) = 0$, a conductive current field is necessarily set up in the plane P_0 as shown by the dashed blue arrows in Fig. 13(c). In the right high-speed zone dominated by the Q_4 events

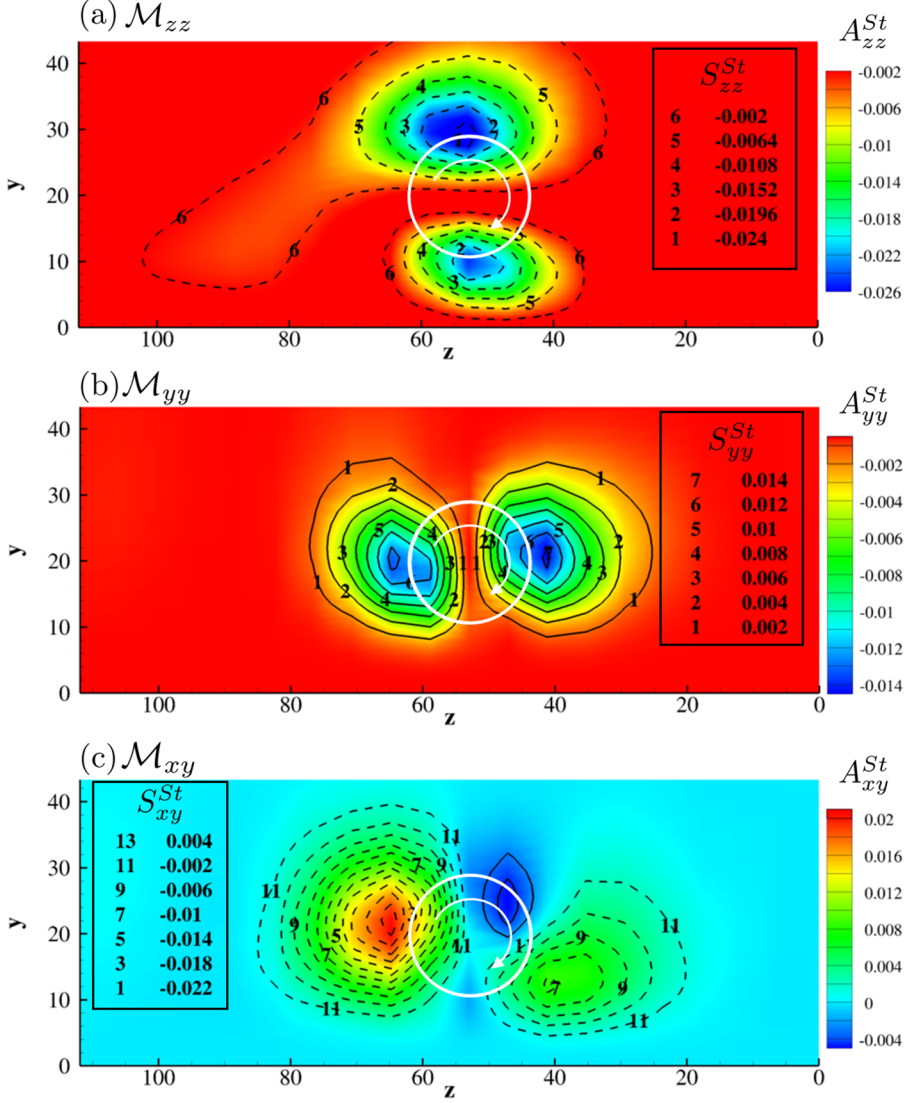


FIG. 12. MHD transport terms of turbulent intensity and Reynolds stress in the P_0 plane for B_x ($\omega_x > 0$). (a) \mathcal{M}_{zz} , contours: $A_{zz}^{St} = -2N_\tau \langle u_z u_z \rangle$; lines: $S_{zz}^{St} = 2N_\tau \langle u_z \frac{\partial \phi}{\partial y} \rangle$. (b) \mathcal{M}_{yy} , contours: $A_{yy}^{St} = -2N_\tau \langle u_y u_y \rangle$; lines: $S_{yy}^{St} = 2N_\tau \langle u_y \frac{\partial \phi}{\partial z} \rangle$. (c) \mathcal{M}_{xy} , contours: $A_{xy}^{St} = -N_\tau \langle u_x u_y \rangle$; lines: $S_{xy}^{St} = N_\tau \langle u_x \frac{\partial \phi}{\partial z} \rangle$. Dashed lines are negative values.

[Fig. 11(c)] wherein $u_x > 0$ one has $j_{c,z} > 0$ (i.e., $\partial \phi / \partial z < 0$), and consequently $\langle u_x \frac{\partial \phi}{\partial z} \rangle < 0$. The same arguments apply in a similar manner to the Q_2 events at the low-speed side of the structure. In these zones, therefore, the source term is $\langle S_{xy}^{St} \rangle < 0$, and it is quasiperfectly opposed to the MHD annihilation term $\langle A_{xy}^{St} \rangle = -N_\tau \langle u_x u_y \rangle$. The same holds true for the Q_3 and Q_1 sites centered, respectively, at $y = 25$ and $y = 10$ in Fig. 11(c).

We now emphasize that the conditional averages of the electromotive and conductive currents are roughly of opposite magnitudes in the plane P_0 , i.e., $\langle j_{em,z} \rangle \approx -\langle j_{c,z} \rangle$, because, again, $\text{div}(\mathbf{j}) = 0$ [Fig. 13(a)]. Since $\mathbf{j}_{em} = \mathbf{u} \times \mathbf{B}$ and $B_x = 1$, here one has $\langle j_{em,z} \rangle = \langle u_y B_x \rangle = \langle u_y \rangle$.

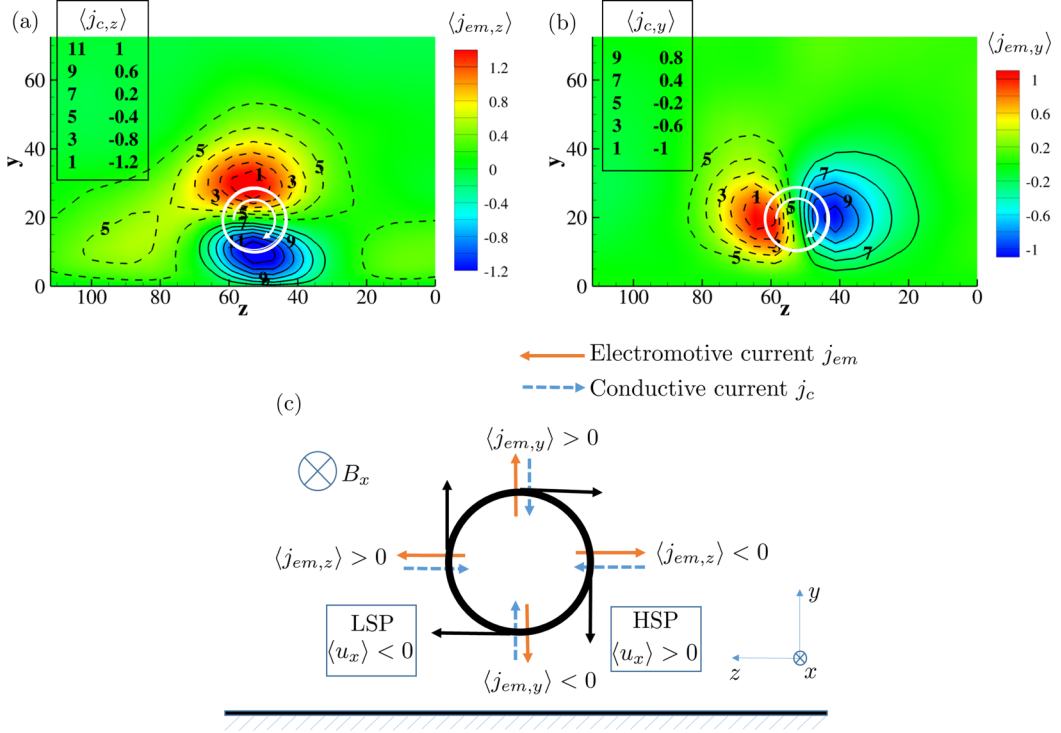


FIG. 13. (a) Contours of spanwise electromotive currents: $\langle j_{em,z} \rangle$. Lines represent spanwise conduction currents $\langle j_{c,z} \rangle$. (b) Contours of wall-normal electromotive currents: $\langle j_{em,y} \rangle$. Lines represent wall-normal conduction currents $\langle j_{c,y} \rangle$. (c) Conceptual model of the electric currents distribution in the plane P_0 of a QSV ($\omega_x > 0$) under a streamwise magnetic field.

Let us assume that $j_{em,z} \approx u_y$, locally near the QSVs. Therefore, $j_{c,z} = -(\frac{\partial \phi}{\partial z}) \approx -u_y$. Recapitulating leads to $N_\tau \langle u_x \frac{\partial \phi}{\partial z} \rangle \approx N_\tau \langle u_x u_y \rangle$, i.e., to the quasiequilibrium between the source and destruction terms. The same approach can be applied to the MHD terms in the wall normal velocity transport $\frac{D u_y u_y}{Dt}$ equation, showing why the net $\langle \mathcal{M}_{ij}^{St} \rangle$ remain weak. Note that these arguments are valid only in or near the median plane P_0 , since the current fields behave differently near or close to the ends of the structure wherein $\frac{\partial \phi}{\partial x}$ is not necessarily negligible.

The topology of the electric current field is different under the spanwise magnetic field. Figures 14(a) and 14(b) show the conditional averages $\langle j_z \rangle$ and $\langle j_y \rangle$ induced by B_z in the P_0 plane. Note that the spanwise current field is purely conductive and $\langle j_z \rangle = -\langle \frac{\partial \phi}{\partial z} \rangle$. A strong negative $\langle j_z \rangle < 0$ field concentrates underneath the structure in the viscous sublayer $y < 5$. This is mainly because of the accumulation of current lines in this zone, as a result of the imposed electrical insulation at the wall. At the top of the vortex, there is a layer of positive lower intensity $\langle j_z \rangle$ extending from the high buffer layer to the logarithmic layer. This is expected since $\int \langle j_z \rangle dx dy dz = 0$. The conditional average $\langle j_y \rangle$, on the other hand, gathers around the high- and low-speed zones of the coherent structure [Fig. 14(b)]. The loop structure of the current field around the QSV is illustrated in Fig. 14(c), showing *inter alia* the setup of the longitudinal current $\langle j_x \rangle$ downstream of the QSV, which is invisible in the plane P_0 .

The conditional averages of the electromotive $\langle j_{em,y} \rangle$ and conductive $\langle j_{c,y} \rangle = -\langle \frac{\partial \phi}{\partial y} \rangle$ currents in the P_0 plane for the B_z case are presented in Fig. 15(a). We again notice the local collapse of

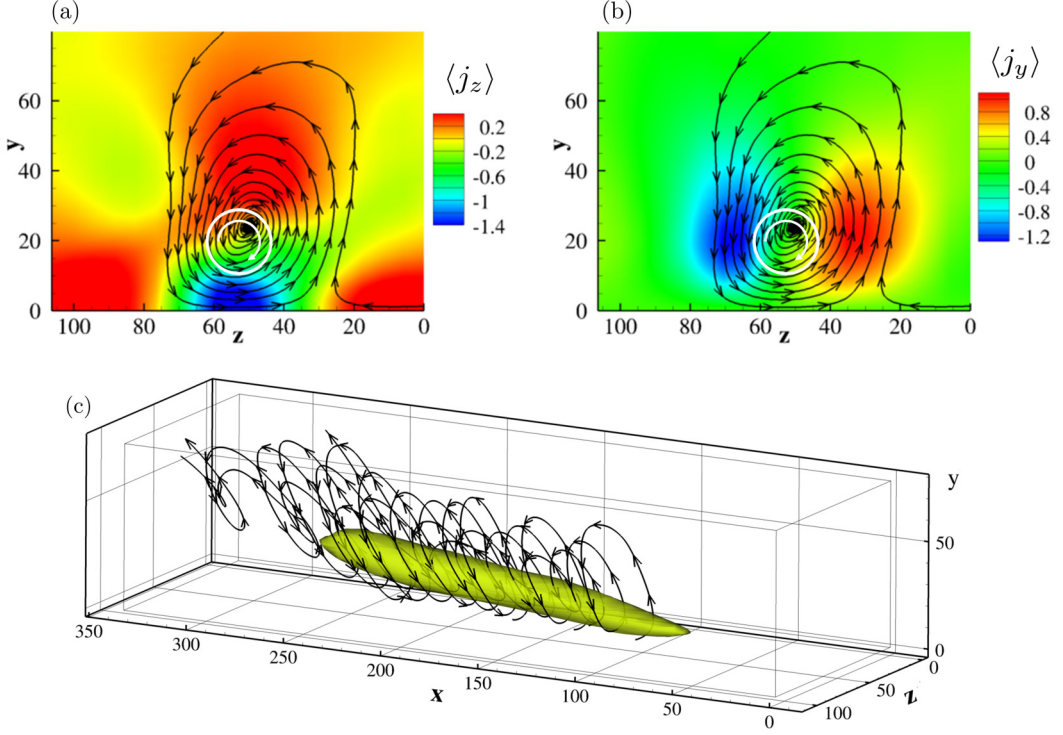


FIG. 14. (a) Spanwise $\langle j_z \rangle$ (composed only of $-\langle \frac{\partial \phi}{\partial z} \rangle$) and (b) wall-normal electric currents contours $\langle j_y \rangle$ in the plane P_0 under a spanwise magnetic field B_z . Both figures show typical electric current lines. (c) Example of 3D electric current lines induced by a QSV ($\omega_x > 0$) under B_z .

electromotive and conductive current fields with $\langle j_{c,y} \rangle \approx -\langle j_{em,y} \rangle$. Figure 15(b) collects all of this information and provides a conceptual model of the current field generated around the QSV.

Let us return again to the shear stress tensor transport mechanism in the light of Fig. 15. Consider $N_\tau \langle u_y \frac{\partial \phi}{\partial y} \rangle$ of the source term in $\langle \mathcal{M}_{xy}^{Sp} \rangle$. The term $-\langle u_x \frac{\partial \phi}{\partial x} \rangle$ will not be discussed, because $\frac{\partial}{\partial x} \approx 0$ along the longitudinal structures, except at the ends. Note, first, $\langle u_y \frac{\partial \phi}{\partial y} \rangle = -\langle u_y j_{c,y} \rangle \approx \langle u_y j_{em,y} \rangle$ is negative, as expected, at both the high- and low-speed sides of the vortex [Figs. 15(b) and 16(a)]. Second, the core of the conditional wall normal velocity $\langle u_y \rangle$ is in the high buffer layer, far from $\langle j_{c,y} \rangle$, which is squeezed in the low buffer layer. This is due to the specific current topology induced by the QSV in the HSP zone. Consequently, the source term $N_\tau \langle u_y \frac{\partial \phi}{\partial y} \rangle$ is small at the right-hand side of the structure [Fig. 16(a)]. At the left LSP side, the conductive current field extends in a larger zone. The size of the latter is limited to about 10 wall units along y and z . It is an easy task to estimate the conditional averages, by noticing that $\langle j_{em,y} \rangle \approx -\langle u_y \rangle$ and that $N_\tau \langle u_y \frac{\partial \phi}{\partial y} \rangle \approx -N_\tau \langle u_y u_y \rangle$. The ratio of the latter to the destruction term $\langle A_{xy}^{Sp} \rangle = -2N_\tau \langle u_x u_y \rangle$ is approximately 10^{-1} in close agreement with Fig. 16(a). In short, the conditional annihilation $\langle A_{xy}^{Sp} \rangle$ term becomes an order of magnitude larger than the source $\langle S_{xy}^{Sp} \rangle$ leading to a net destruction of the shear stress by direct MHD effects as discussed in the previous section.

We underlined the strong MHD damping effect on the turbulent wall normal velocity transport in the previous section [Fig. 10(d)]. The conditional destruction term $\langle A_{yy}^{Sp} \rangle = -2N_\tau \langle u_y u_y \rangle$ is directly related to the coherent wall normal velocity intensity, therefore the interpretation of the Fig. 16(b) is straightforward. What is striking, on the other hand, is to note that $\langle A_{yy}^{Sp} \rangle$ reaches values up to five times the local mean dissipation ε_{yy} at $y \approx 20$, particularly at the HSP side. Moreover, the source

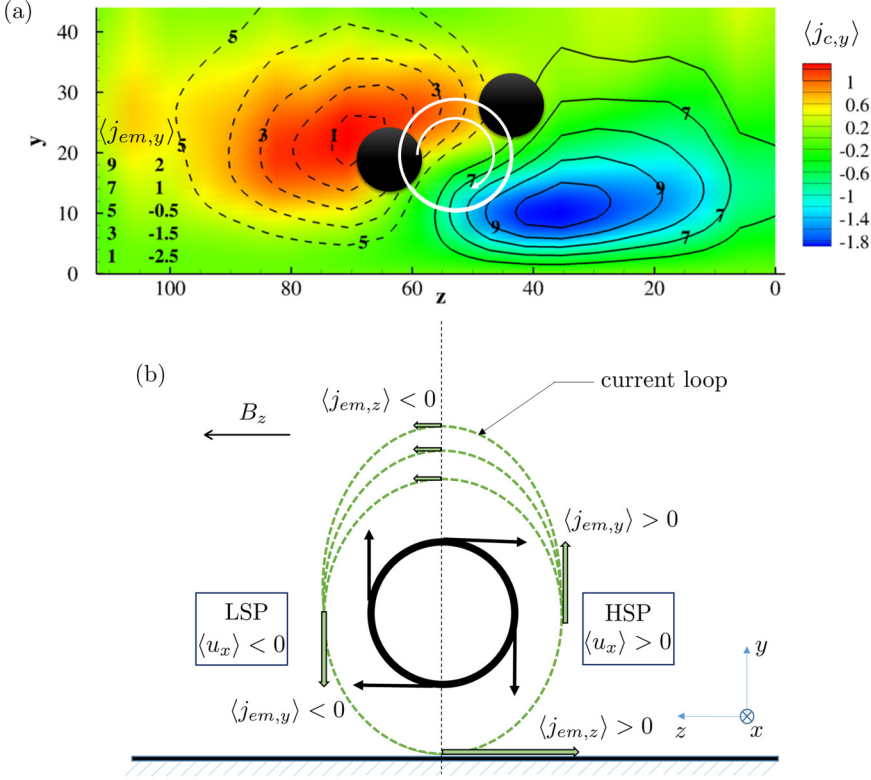


FIG. 15. (a) Wall-normal electrical current contributions under B_z . Contours: $\langle j_{c,y} \rangle$, lines: $\langle j_{em,y} \rangle$. Black spots are the positions of extreme values of wall normal fluctuating velocities u_y . (b) Conceptual model of the electric currents distribution in the plane P_0 of a QSV ($\omega_x > 0$) under a spanwise magnetic field.

term $\langle S_{yy}^{Sp} \rangle = -2N_\tau \langle u_y \frac{\partial \phi}{\partial x} \rangle$ remains weak around the structure, again because $\frac{\partial}{\partial x} \approx 0$ along the QSV as indicated before.

V. CONCLUDING REMARKS

Conditional averages of both the electric current field and the directly implied MHD shear stress transport terms educed near the inner layer coherent eddies are significantly different under the streamwise and the spanwise magnetic fields. A clear understanding of the electric field behavior requires its decomposition into electromotive and conductive parts. The electromotive current induced near the quasilonitudinal vortices is quasibalanced by the conductive current under B_x . This is a direct consequence of the solenoidal feature of the electric current. The resulting total current intensity is therefore low. The streamwise magnetic field B_x is, *in fine*, not efficient enough to alter the near wall turbulence structures, while at equivalent Stuart numbers the spanwise field already relaminarizes the flow. The electric current field topologies are significantly different under B_z than under B_x . We have shown that B_z generates a net electric current around the structures, in the opposite direction to their rotations. At the same time, a conductive current field accumulates in the viscous sublayer because of the electrical insulation at the wall. It has to be emphasized here that these hidden peculiarities were able to be analyzed due to the conditional averages educed from the active coherent structures.

Annihilation and source terms which are directly related to the magnetic field emerge from the shear stress transport equations. The magnetic field destruction of the Reynolds shear stress

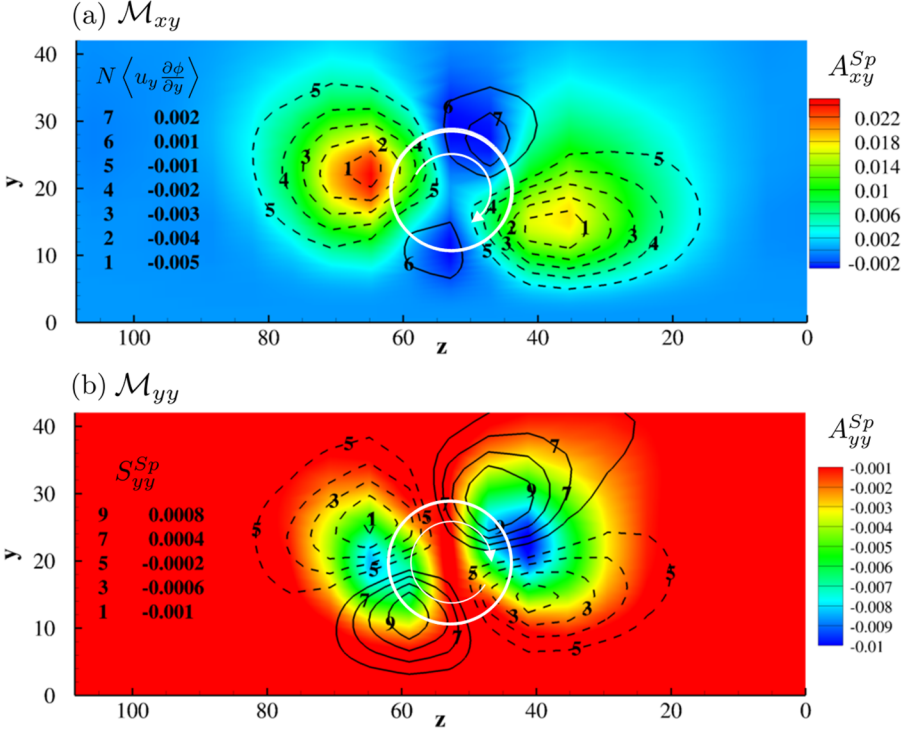


FIG. 16. MHD transport terms of turbulent intensity and Reynolds stress in the P_0 plane for B_z ($\omega_x > 0$). (a) \mathcal{M}_{xy} , contours: $A_{xy}^{Sp} = -2N_\tau \langle u_x u_y \rangle$; lines: $N_\tau \langle u_y \frac{\partial \phi}{\partial y} \rangle$. (b) \mathcal{M}_{yy} , contours: $A_{yy}^{Sp} = -2N_\tau \langle u_y u_y \rangle$; lines: $S_{yy}^{Sp} = -2N_\tau \langle u_y \frac{\partial \phi}{\partial x} \rangle$. Dashed lines are negative values.

overcomes its MHD source counterpart under B_z independently of the Stuart number. Small enough Stuart numbers are then sufficient for the net MHD destruction to become comparable to the production of the Reynolds shear stress. That leads to a rapid flow relaminarization, once N_τ exceeds a critical threshold of about 6×10^{-3} . The source terms induced by the streamwise magnetic field impedes the drag reduction. The net destruction of the shear stresses by direct MHD effects requires an order of magnitude larger Stuart numbers under B_x than B_z . The B_x field first attenuates the wall normal turbulent velocity intensity, contrarily to B_z , which directly attacks $\overline{u_x u_y}$. Basically this is a slower process, and the relaminarization is delayed to much larger N_τ under B_x .

ACKNOWLEDGMENTS

The authors would like to acknowledge the support of the Labex TEC21 (Grant No. ANR-11-LABX-0030). Most of the computations presented in this paper were performed using the Froggy platform of the CIMENT infrastructure [31], which is supported by the Rhône-Alpes region (GRANT CPER07-13 CIRA) and the Equip@Meso project (reference ANR-10-EQPX-29-01) of the programme Investissements d’Avenir supervised by the Agence Nationale pour la Recherche.

APPENDIX: COMPUTATIONAL DETAILS

Supplementary details on the direct numerical simulations are provided here. We recall that the mesh nodes are distributed uniformly along x and z and refined near the wall in the wall-normal y direction. The mesh size Δy is set to one third of the Kolmogorov scale η near the wall while $\Delta y \approx \eta$ at the centerline. The y coordinate for the j th node is obtained from a uniform distribution

$s(j) = \frac{(j-1)}{n_y}$ (where n_y stands for the total node number in the wall normal direction) modified through the following expression:

$$y(j) = 2 \frac{\tanh\left[\alpha s(j) - \frac{1}{2}\right]}{\tanh\left(\frac{\alpha}{2}\right)}, \quad (\text{A1})$$

where $\alpha = 0.38$ controls the intensity of the refinement near the boundaries. A Jacobian approach is used to evaluate the derivatives along the y direction. The first and second derivatives used for convective and diffusive terms are then given by

$$\frac{\delta f}{\delta y} = \frac{ds}{dy} \frac{\delta f}{\delta s}, \quad \frac{\delta f}{\delta y} = \frac{d^2 s}{dy^2} \frac{\delta f}{\delta s} + \left(\frac{ds}{dy}\right)^2 \frac{\delta^2 f}{\delta s^2}, \quad (\text{A2})$$

where δ denotes spatial derivatives estimations. The coefficients related to the mesh geometry, $\frac{ds}{dy}$ and $\left(\frac{ds}{dy}\right)^2$, found in Eq. (A2) are evaluated analytically from the relation (A1). Considering the temporal flow evolution, the solution at the next time (sub)iteration $k + 1$ is explicitly obtained by integrating Eq. (3). The time interval $[t, t + \Delta t]$ is then divided into n_k substeps ($t_1 = t, t_2, \dots, t_{n_k} = t + \Delta t$).

By applying the fractional step method, the velocity is corrected to become solenoidal for each time iteration. Making use of the conventional Einstein notation for spatial coordinate and velocity components (for which subscripts 1,2,3 refer respectively to the spanwise z , wall-normal y , and streamwise x component), the temporal advancement of Eq. (3) can be expressed as

$$\mathbf{u}^{k+1} = \mathbf{u}^k + \mathbf{T}_{\text{pmean}} + \mathbf{T}_{\text{pfloc}} + \mathbf{T}_{\text{adv}} + \mathbf{T}_{\text{diff}} + \mathbf{T}_{\text{fext}}, \quad (\text{A3})$$

where

$$\begin{aligned} \mathbf{T}_{\text{pmean}} &= - \int_{t_k}^{t_{k+1}} \left(\frac{\partial \bar{p}}{\partial x_i} \right) dt, & \mathbf{T}_{\text{pfloc}} &= - \int_{t_k}^{t_{k+1}} \frac{\partial p'}{\partial x_i} dt, & \mathbf{T}_{\text{adv}} &= - \int_{t_k}^{t_{k+1}} \frac{\partial u_i u_j}{\partial x_j} dt, \\ \mathbf{T}_{\text{diff}} &= \int_{t_k}^{t_{k+1}} \frac{\partial^2 u_i}{\partial x_j^2} dt, & \mathbf{T}_{\text{fext}} &= N_\tau \int_{t_k}^{t_{k+1}} \epsilon_{ijm} (j_j \cdot B_m) dt; \end{aligned}$$

ϵ_{ijk} is the Levi-Civita operator. $\left(\frac{\partial \bar{p}}{\partial x_i}\right)$ and $\frac{\partial p'}{\partial x_i} dt$ stand, respectively, for the mean gradient pressure and the pressure gradient fluctuation. $\mathbf{T}_{\text{pmean}}$ is evaluated through the global flow rate conservation. The advection, diffusion, and external force terms, respectively, \mathbf{T}_{adv} , \mathbf{T}_{diff} , and \mathbf{T}_{fext} , are estimated explicitly from previous $k - 1$ and the current k fields as

$$\begin{aligned} \mathbf{T}_{\text{adv}} + \mathbf{T}_{\text{diff}} + \mathbf{T}_{\text{fext}} &= \alpha_k \Delta t \left(- \frac{\partial \widehat{u_i u_j}}{\partial x_j} + \frac{\partial^2 \widehat{u_i}}{\partial x_j^2} + N_\tau \epsilon_{ijm} \widehat{(j_j \cdot B_m)} \right)_k \\ &\quad + \beta_k \Delta t \left(- \frac{\partial \widehat{u_i u_j}}{\partial x_j} + \frac{\partial^2 \widehat{u_i}}{\partial x_j^2} + N_\tau \epsilon_{ijm} \widehat{(j_j \cdot B_m)} \right)_{k-1}, \end{aligned} \quad (\text{A4})$$

where $\widehat{(\cdot)}$ denotes spatially discretized operators.

The term $\epsilon_{ijm} (j_j \cdot B_m)$ depends on the velocity field u_i and the electric potential ϕ . The time advancement is performed by a Runge-Kutta third-order (RK3) scheme in which the coefficients involved in the three iteration steps are $\alpha_{1,2,3} = \left[\frac{8}{15}, \frac{5}{12}, \frac{3}{4}\right]$ and $\beta_{1,2,3} = \left[0, -\frac{17}{60}, -\frac{5}{12}\right]$. $\mathbf{T}_{\text{pfloc}}$ is the fluctuating pressure gradient evaluated from the pressure at $k + 1$. Indeed, Eq. (A3) can be reformulated as

$$\mathbf{u}^{k+1} = \widetilde{\mathbf{u}}^{k+1} - (\alpha_k + \beta_k) \Delta t \widehat{\nabla p^{k+1}}, \quad (\text{A5})$$

where $\widetilde{\mathbf{u}}^{k+1} = \mathbf{u}^k + \mathbf{T}_{\text{pmean}} + \mathbf{T}_{\text{adv}} + \mathbf{T}_{\text{diff}}$ is a first estimation of the velocity field, based on terms known at the current time iteration. The quantity p^{k+1} is then calculated by applying the divergence-

free operator to Eq. (A5) and solving the resulting Poisson equation:

$$\widehat{\nabla^2 p'^{k+1}} = \frac{1}{\Delta t(\alpha_k + \beta_k)} \widehat{\nabla \cdot \tilde{u}^{k+1}}. \quad (\text{A6})$$

The Poisson equation for the pressure is solved in the Fourier domain (through FFT decomposition) at each $[x, z]$ plane.

For each time step, the iteration procedure derived from the RK3 time resolution of the $[\phi, u_i]$ coupling is then the following:

(1) Compute ϕ^k from the current velocity field u^k by solving the current conservation equation [Eq. (4)]: $\widehat{\nabla^2 \phi^k} = \widehat{\nabla \cdot \epsilon_{ijm} u^k B_m}$

(2) Compute $\mathbf{T}_{\text{adv}} + \mathbf{T}_{\text{diff}} + \mathbf{T}_{\text{fext}}$ from previous and current fields estimations

(3) Correct the velocity field \tilde{u}^{k+1} [see Eq. (A5)] by solving the Poisson equation (A6).

It is worth noting that no additional iteration procedure is required to solve the two-way coupling of the ϕ and u_i through the steps 1–3 since the time step for solving turbulent wall bounded flow by an explicit time advancement scheme is necessarily very small.

-
- [1] F. W. Fraim and W. H. Heiser, The effect of a strong longitudinal magnetic field on the flow of mercury in a circular tube, *J. Fluid Mech.* **33**, 397 (1968).
 - [2] P. S. Lykoudis and E. C. Brouillette, Magneto-fluid-mechanic channel flow. II. Theory, *Phys. Fluids* **10**, 1002 (1967).
 - [3] R. A. Gardner and P. Lykoudis, Magneto-fluid-mechanic pipe flow in a transverse magnetic field. Part 1. Isothermal flow, *J. Fluid Mech.* **47**, 737 (1971).
 - [4] C. B. Reed and P. Lykoudis, The effect of a transverse magnetic field on shear turbulence, *J. Fluid Mech.* **89**, 147 (1978).
 - [5] H. Branover and P. Gershon, Experimental investigation of the origin of residual disturbances in turbulent MHD flows after laminarization, *J. Fluid Mech.* **94**, 629 (1979).
 - [6] D. Lee and H. Choi, Magnetohydrodynamic turbulent flow in a channel at low magnetic Reynolds number, *J. Fluid Mech.* **439**, 367 (2001).
 - [7] D. S. Krasnov, E. Zienicke, O. Zikanov, T. Boeck, and A. Thess, Numerical study of the instability of the Hartmann layer, *J. Fluid Mech.* **504**, 183 (2004).
 - [8] T. Boeck, D. Krasnov, and E. Zienicke, Numerical study of turbulent magnetohydrodynamic channel flow, *J. Fluid Mech.* **572**, 179 (2007).
 - [9] J. A. Shercliff, *A Textbook of Magnetohydrodynamics* (Pergamon Press, Oxford, 1965).
 - [10] V. Shatrov and G. Gerbeth, Marginal turbulent magnetohydrodynamic flow in a square duct, *Phys. Fluids* **22**, 084101 (2010).
 - [11] H. Kobayashi, Large eddy simulation of magnetohydrodynamic turbulent duct flows, *Phys. Fluids* **20**, 015102 (2008).
 - [12] J. Jimenez and A. Pinelli, The autonomous cycle of near-wall turbulence, *J. Fluid Mech.* **389**, 335 (1999).
 - [13] J. Jiménez, Coherent structures in wall-bounded turbulence, *J. Fluid Mech.* **842**, P1 (2018).
 - [14] S. F. Tardu, in *Wall Turbulence Control* (John Wiley and Sons, New York, 2017).
 - [15] T. Boeck and D. Krasnov, A mixed length model for side layers of magnetohydrodynamic channel and duct flows with insulating walls, *Phys. Fluids* **26**, 025106 (2014).
 - [16] D. Krasnov, M. Rossi, O. Zikanov, and T. Boeck, Optimal growth and transition to turbulence in channel flow with spanwise magnetic field, *J. Fluid Mech.* **596**, 73 (2008).
 - [17] A. Potherat and K. Kornet, The decay of wall-bounded MHD turbulence at low Rm, *J. Fluid Mech.* **783**, 605 (2015).
 - [18] F. Bauer, S. F. Tardu, and O. Doche, Efficiency of high accuracy DRP schemes in direct numerical simulations of incompressible turbulent flows, *Comput. Fluids* **107**, 123 (2015).

- [19] J. Schillings, O. Doche, F. Bauer, J. Deseure, M. T. Retamales, and S. Tardu, Four-way coupled Eulerian-Lagrangian direct numerical simulations in a vertical laminar channel flow, *Int. J. Multiphase Flow* **89**, 92 (2017).
- [20] C. K. W. Tam and J. C. Webb, Dispersion-relation-preserving finite difference schemes for computational acoustics, *J. Comput. Phys.* **107**, 262 (1993).
- [21] D. Krasnov, O. Zikanov, J. Schumacher, and T. Boeck, Magnetohydrodynamic turbulence in a channel with spanwise magnetic field, *Phys. Fluids* **20**, 095105 (2008).
- [22] P. Orlandi, Drag reduction in turbulent MHD pipe flows, in *CTR Proceedings of the Summer Program* (NASA-Ames Research Center and Stanford University, 1996), pp. 447–456.
- [23] A. B. Tsinober, MHD-Drag Reduction, in *Viscous Drag Reduction in Boundary Layers*, edited by D. M. Bushnell and J. N. Hefner, AIAA Prog. Astron. Aeron. Series (AIAA, Reston, VA, 1990), Vol. 123, pp. 327–349.
- [24] N. Mansour and P. Moin, Reynolds-stress and dissipation-rate budgets in a turbulent channel flow, *J. Fluid Mech.* **194**, 15 (1988).
- [25] I. Marusic, J. Monty, M. Hultmark, and A. Smits, On the logarithmic region in wall turbulence, *J. Fluid Mech.* **716**, R3 (2013).
- [26] S. Hoyas and J. Jimenez, Scaling of the velocity fluctuations in a turbulent channel up to $Re_\tau = 2003$, *Phys. Fluids* **118**, 011702 (2006).
- [27] K. Fukagata, K. Iwamoto, and N. Kasagi, Contribution of the Reynolds stress distribution to the skin friction in wall-bounded flows, *Phys. Fluids* **14**, L73 (2002).
- [28] S. F. Tardu, in *Transport and Coherent Structures in Wall Turbulence* (John Wiley and Sons, New York, 2014).
- [29] J. Jeong and F. Hussain, On the identification of a vortex, *J. Fluid Mech.* **285**, 69 (1995).
- [30] J. Jeong, W. S. F. Hussain, and J. Kim, Coherent structures near the wall in a turbulent channel flow, *J. Fluid Mech.* **332**, 185 (1997).
- [31] <https://ciment.ujf-grenoble.fr>.